Article

Wide-Field Mid-Infrared Hyperspectral Imaging by Snapshot Phase Contrast Measurement of Optothermal Excitation

Tao Yuan, Miguel A. Pleitez,* Francesca Gasparin, and Vasilis Ntziachristos*

Cite This: *Anal. Chem.* 2021, 93, 15323−15330

Read Online

ACCESS | Metrics & More | Article Recommendations | SI Supporting Information

ABSTRACT: Vibrational microscopy methods based on Raman scattering or infrared absorption provide a label-free approach for chemical-contrast imaging, but employ point-by-point scanning and impose a compromise between the imaging speed and field-of-view (FOV). Optothermal microscopy has been proposed as a promising imaging modality to avoid this compromise, although at restrictively small FOVs capable of imaging only few cells. Here, we present wide-field optothermal mid-infrared microscopy (WOMiM) for wide-field chemical-contrast imaging based on snapshot pump−probe detection of optothermal signal, using a custom-made condenser-free phase contrast microscopy to capture the phase change of samples after mid-infrared irradiation. We achieved chemical contrast for FOVs up to 180 μm in diameter, yielding 10-fold larger imaging areas than the state-of-the-art, at imaging speeds of 1 ms/frame. The maximum possible imaging speed of WOMiM was determined by the relaxation time of optothermal heat, measured to be 32.8 μs in water, corresponding to a frame rate of ∼30 kHz. This proof-of-concept demonstrates that vibrational imaging can be achieved at an unprecedented imaging speed and large FOV with the potential to significantly facilitate label-free imaging of cellular dynamics.
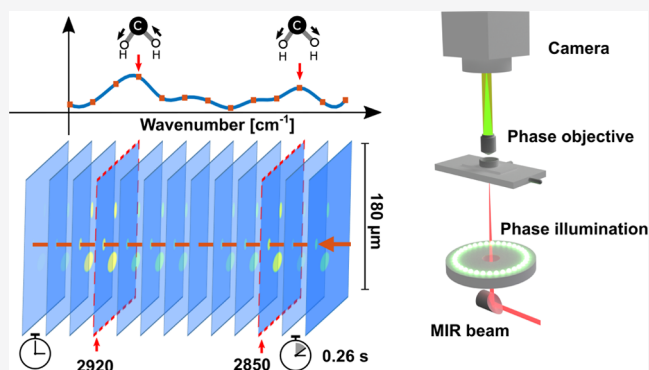
1. INTRODUCTION

Live-cell chemical-contrast microscopy based on vibrational excitation of biomolecules can reveal cell metabolism dynamics in a label-free manner and includes coherent anti-Stokes Raman scattering (CARS) microscopy, stimulated Raman scattering microscopy, and (recently) mid-infrared (MIR) optoacoustic microscopy (MiROM).[1−3] However, these modalities rely mainly on image acquisition via point-by-point raster scanning[4−6] which imposes a compromise between the imaging speed and field-of-view (FOV). In particular, the raster scanning method is not suitable for imaging fast dynamic changes, such as lipid droplet movement along microtubules with velocities ranging in the μm/s[7−9] or action potentials in neurons which occur in the range of milliseconds.[10] This is especially limiting when imaging big cells (e.g., adipocytes can be up to 100 μm in size[11]) or large cell populations (hundreds to thousands of cells) needed to obtain statistically relevant analysis. A strategy to increase the imaging speed at large FOVs has been to increase the scanning step size (for instance, 5−20 μm); however, this practice notably reduces the overall imaging resolution. For hyperspectral imaging (i.e., imaging at multiple wavelengths), low imaging speed imposes a compromise between the FOV and spectral coverage; that is, the bigger the scanning FOV, the smaller the wavelength range that can be covered within a given time. Additionally, although galvo scanners enable an imaging speed of up to 30 frames/s,

they suffer from imaging distortion in large FOVs as the scanning beam shifts away from the optical axis. Therefore, there is a need for alternative methods to achieve high-speed chemical-contrast imaging of fast and dynamic cellular changes for large FOVs at wide spectral range and high spatial resolution.

To avoid the compromise between imaging speed, FOV, spectral coverage, and resolution, various wide-field vibrational microscopy methods for high-speed chemical-contrast imaging have recently been proposed.[12−16] For instance, wide-field CARS microscopy, where a vibrational image is obtained by expanding the Stokes and pump beam, achieved video-rate imaging using spectral coverage of four excitation wavelengths.[12] Similarly, quantitative optothermal microscopy, where optothermally induced phase changes are quantitatively measured for chemical-contrast imaging, has achieved imaging speeds up to 10 ms/frame (before averaging) for imaging of intracellular structures, such as nuclei and lipid droplets.[13,15]
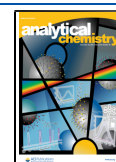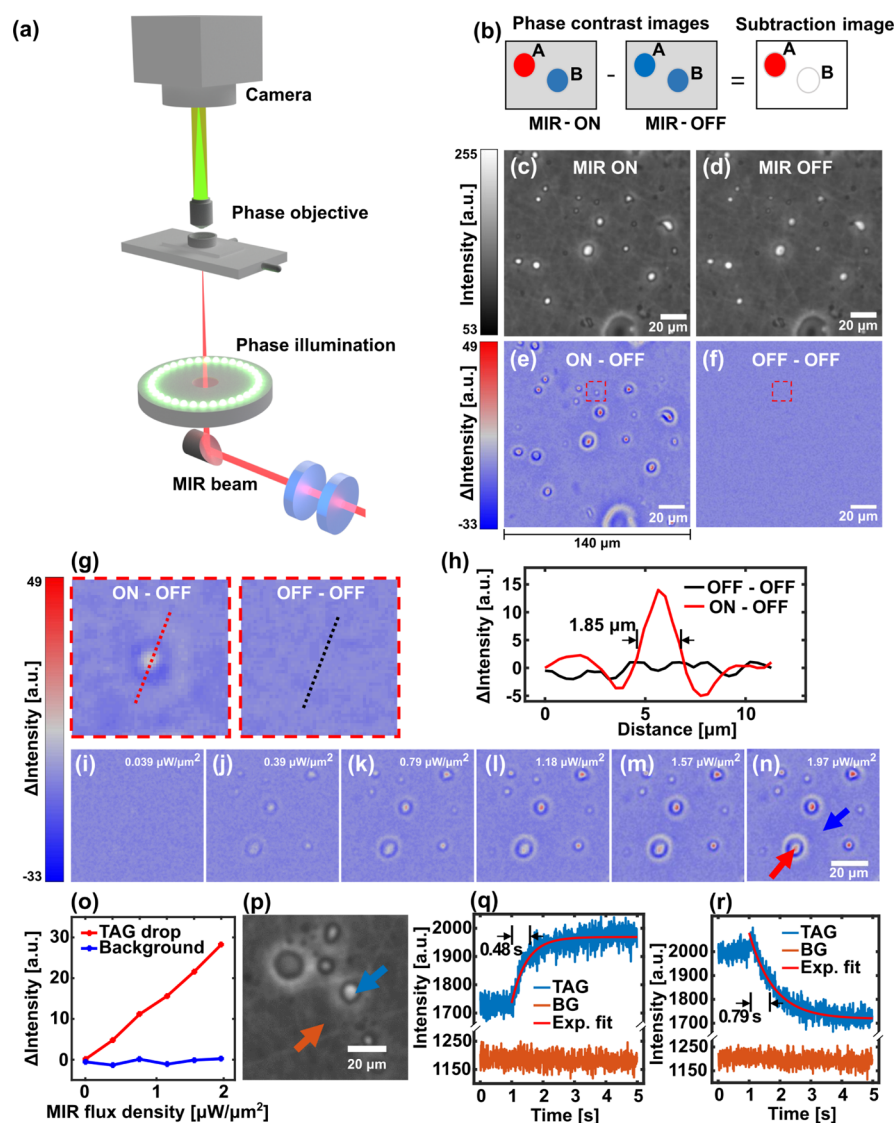
Figure 1. Operational principle and characterization of WOMiM. (a) Schematic of WOMiM. MIR pulses are focused on the sample by a parabolic mirror. The phase change due to MIR absorption is obtained by capturing MIR-ON and MIR-OFF micrographs with a CPCM. (b) Chemical-contrast image is obtained by subtracting a MIR-OFF image from a MIR-ON image. (c) MIR-ON image (MIR wavenumber at 2850 cm^{-1}) and (d) MIR-OFF image of TAG drops. (e) WOMiM micrograph by subtracting (d) from (c). (f) Subtraction of two MIR-OFF images. (g) Zoom-in FOVs of the smallest observed TAG drop, as marked by the red dash rectangles in (e,f). (h) Line profiles of the smallest observed TAG drop in (g). (i−n) Illustrations of WOMiM micrographs (subtraction images) at varying MIR excitation flux density (0.039−1.97 $\mu W/\mu m^2$). (o) Intensity plot of a TAG drop center and an arbitrary point in the background as indicated by red and blue arrows in (n). (p−r) Intensity variation plots as the MIR was turned on at 1 s (q) and turned off at 1 s (r), where the intensity is acquired at the location of the two arrows in (p).

However, both wide-field CARS and quantitative optothermal microscopy are limited to small chemical-contrast FOVs of 10−50 μm (FOVs refer to the diameter of the excitation area), whereas FOVs above 100 μm are necessary for imaging cell populations or big cells. Quantitative measurements of phase changes usually rely on complex optics that are susceptible to vibration, making it challenging for detecting the subtle phase change after expansion of the MIR excitation area (due to lower flux density). A recent MIR microscopy method based on a nonlinear interferometer was proposed as a large FOV imaging modality, demonstrating an up to 1.2 mm FOV for the imaging of paraffin-embedded tissue slices at a single MIR wavelength.[16] The function of a nonlinear interferometer relies on spontaneous parametric down-conversion (SPDC) of a nonlinear crystal. Here, a pump photon is converted into two low energy photons (an idler photon and a signal photon),

where the idler photons are used to probe the sample and the signal photons are detected by a camera.[17−19] However, the conversion efficiency of SPDC is typically low, as only a limited number of signal photons reach the detector, resulting in a low signal-to-noise-ratio (SNR).

We hypothesized that chemical-contrast imaging at large FOVs and high speeds can be achieved by probing the phase contrast change using a custom-made condenser-free phase contrast microscope (CPCM).[20,21] A sample is first imaged by a CPCM (MIR-OFF) and subsequently imaged in the same way under MIR irradiation (MIR-ON). Chemical-contrast micrographs are obtained by the difference in MIR-OFF/MIR-ON phase contrast images. Here, acquisition of chemical-contrast images no longer relies on point-by-point raster scanning, and the FOV is determined by the size of the MIR-
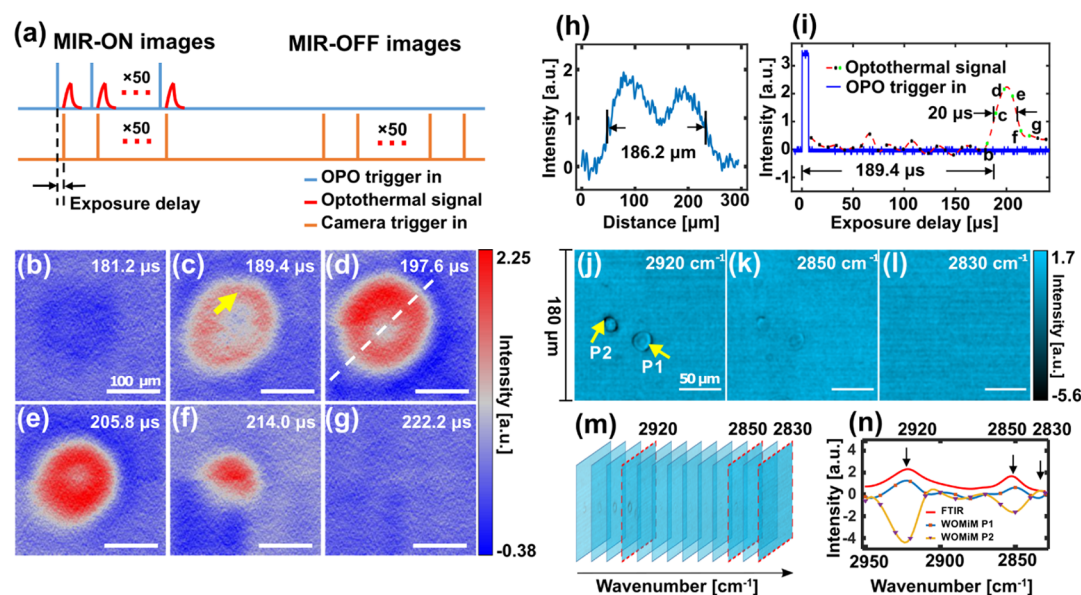
Figure 2. Imaging of optothermal signal in water and hyperspectral imaging of TAG drops. (a) Schematic diagram of a pulse train for single-pulse-level synchronization. In this synchronization mode, each single MIR-ON image is captured as a MIR pulse arrives. The corresponding MIR-OFF image is later captured when the OPO trigger stops. (b−g) Illustration of subtraction images with the exposure delay varying from 181.2 to 222.2 μs. Each image is a subtraction of 50-averaged MIR-ON and 50-averaged MIR-OFF phase images. (h) Line profile across the 2D optothermal signal (hot spot) for characterization of the MIR excitation area in (d). Line profile suggests a full width at half-maximum of 186.2 μm for the diameter of MIR excitation area. (i) Plot of "OPO trigger in" and the optothermal signal, where the optothermal signal is the z-profile of a pixel [indicated in (c)] from an image stack (exposure delay varies from 9 to 238.6 μs with a step size of 8.2 μs). Dots (black or green): original data from the image stack. Red dashed line: cubic spline interpolation. The green dots in (i) correspond to values from six images in (b−g) labeled "(b)" to "(g)". (j−l) Three selected images from a hyperspectral image stack. Scale bar = 50 μm. (m) Hyperspectral image stack. The wavenumber varies from 2950 to 2830 cm^{-1} with a step size of 10 cm^{-1}. (n) WOMiM spectra of selected points as indicated by the arrows in (j), and the corresponding TAG spectrum measured by Fourier transform infrared (FTIR) spectroscopy. In the WOMiM spectra, smooth lines are obtained using cubic spline interpolation. In (b−g) and (j−l), dark current noise of camera was filtered out by Gaussian blurry.

excited area as well as by the imaging area of the phase contrast microscope.

To this end, we introduce wide-field optothermal mid-infrared microscopy (WOMiM), which uses MIR beams to selectively induce refractive index changes on samples due to the optothermal effect (i.e., heat deposition due to optical absorption). Localized and selective refractive index changes were probed by CPCM. Benefiting from the robustness of CPCM, we were able to detect the phase difference after extending the MIR excitation area up to 180 μm in diameter, which translates to an imaging area approximately 36 times larger than in wide-field CARS microscopy (FOV ∼30 μm)[12,22] and 10 times larger than in quantitative wide-field optothermal microscopy (FOV ∼50 μm).[13,15] By means of WOMiM, we were able to obtain wide-field chemical-contrast images (for a FOV of ca. 180 μm) of triglyceride (TAG) drops in water within 1 ms, which is ∼20 times faster than point-by-point scanning methods using galvo-resonant scanners with a comparable FOV of 180 μm, and 10 times faster than other recently reported quantitative optothermal microscopy modalities even at a smaller FOV of 50 μm.[13,15] Collectively, we demonstrate a proof-of-concept of the proposed method by high-speed chemical-contrast imaging of TAG drops and water, paving the way toward real-time monitoring of cellular dynamics.

2. EXPERIMENTAL SECTION

2.1. Experimental Setup. A 9 ns pulse width MIR optical parametric oscillator (OPO) laser (NT277, EKSPLA; 1 kHz pulse repetition rate) was used as the MIR pump source. The output of OPO laser was then passed through a germanium window and a MIR polarizer, for the purpose of filtering out the visible signal beam generated by the parametric process and adjusting the MIR irradiation power. The MIR (idler beam) was then focused by a low numerical aperture (NA) gold parabolic mirror (#37248, Edmund Optics Ltd.; NA = 0.062) on the sample, creating a focus spot of 186.2 μm in diameter (at 3480 cm^{-1}). A custom-made Petri dish with a ZnS window (4ZNS F2505, Crystal GmbH) on the bottom was used to hold the samples. The change of phase due to MIR absorption was probed by a custom-made CPCM, in which an annular illuminator (Aura, Cairn Research Ltd.) was used for phase illumination to facilitate the MIR irradiation. The annular illuminator was placed below a phase objective (20×, Nikon; NA = 0.4) in a conjugate plane of the objective phase ring to fulfill the condition for phase contrast imaging. A high-speed camera (PCO.dimax cs4, PCO AG) was used on the microscope to acquire the phase images (MIR-ON/MIR-OFF). Both the camera and OPO laser were externally triggered by a programmable microcontroller (MSP430, Texas Instruments Inc.). The camera, OPO laser, and micro-controller were connected to the computer and the whole system can be operated by a custom-made MATLAB user interface.

2.2. Sample Preparation. Using a 10 mg/mL solution of 1,2-dioleoyl-3-palmitoyl-rac-glycerol (Sigma-Aldrich Inc.), TAG drops were prepared by dissolving 1 mg of this solution in 100 μL of a chloroform−methanol solution (2:1). 10 μL of the TAG solution was placed on a custom-made Petri dish with a ZnS window and left to dry at room temperature until

complete evaporation of chloroform−methanol, leaving the TAG drops on the surface of the ZnS window. The TAG drop sample was then used for proof-of-concept measurements as shown in Figure 1. Water-immersed TAG drops (Figure 2j−m) were prepared by adding a 1 mm layer of deionized water and covered with cover glass (0.17 mm thick) to reduce water evaporation and maintain the thickness of the water layer. Optothermal signal characterization (Figure 2b−i) was performed in a layer of 1 mm of water, detecting the signal from water between the ZnS and cover glass.

2.3. Image Acquisition Settings. In proof-of-concept measurements (Figure 1c−f) or characterization of linearity (Figure 1i−n), MIR-ON/MIR-OFF phase contrast images were acquired by a monochromatic CMOS camera (FL3-U3-20E4M-C, FLIR Systems Inc.). Using on-off-level synchronization, the MIR-ON phase images were captured 4 s after OPO switch-on and MIR-OFF phase images were captured 4 s after OPO switch-off. Both the exposure time of MIR-ON and MIR-OFF phase images were set to 250 ms. To acquire MIR-ON images for the TAG drops, the OPO was tuned to the CH symmetry stretch vibration peak of 2850 cm^{-1} in wavenumber,[23] with an excitation flux density of 0.64 $\mu W/\mu m^2$ on the sample.

A high-speed camera (PCO.dimax cs4, PCO AG) was used for the characterization of the optothermal process (Figure 1p−r for TAG drops and Figure 2b−g for water) and hyperspectral imaging measurement (Figure 2j−l). Both the characterization of water optothermal process (Figure 2b−g) and hyperspectral imaging (Figure 2j−m) applied single-pulse-level synchronization, in which MIR-ON and MIR-OFF images were captured at a frame rate of 1 kHz with an exposure time of 5.5 μs. During characterization of the water optothermal process, the OPO was tuned to a high absorption wavelength of water (3480 cm^{-1} in wavenumber) with an excitation flux density of 1.64 $\mu W/\mu m^2$ on the sample. A subtraction image was obtained by subtracting the average of 50 MIR-ON images from the average of 50 MIR-OFF phase images. To scan the whole process of optothermal signal, the exposure delay of MIR-ON images was set to a particular sequence (start: 9 μs; step: 8.2 μs; stop: 993 μs), resulting in 121 subtraction images. In hyperspectral imaging, the exposure delay was fixed to a value (194.0 μs) that yielded the maximum optothermal signal. The wavenumber of the OPO was tuned from 2830 to 2950 cm^{-1} with a step size of 10 cm^{-1}. An average of 18 MIR-ON phase images and 18 MIR-OFF phase images were used for obtaining a subtraction image.

2.4. Data Processing. ImageJ was used for calculating subtraction images and extracting line profiles in the proof-of-concept measurement (Figure 1e,f,i−n). MATLAB was used to perform an exponential fit of the optothermal process of TAG drops and plotting the profile and spectra figures. For hyperspectral imaging, a graphical user interface based on MATLAB App Designer was developed for OPO wavelength tuning, synchronization setting, images acquisition, and other options. A Gaussian smooth (radius = 2) was applied as shown in Figure 2b−g,j−l to remove the camera hot pixels and dark current noise. Cubic spline interpolation was applied to the WOMiM spectra as shown in Figure 2n.

3. RESULTS

3.1. Imaging Principle and Proof-of-Concept. Figure 1a depicts the schematic representation of WOMiM. In this system, a custom-made CPCM was used to probe the phase

change due to MIR absorption. The phase contrast performance of the CPCM was characterized both experimentally and by using simulations (see Figure S1). MIR pulses were focused by a low NA parabolic mirror, creating a wide excitation area (ca. 180 μm in diameter) on the sample. The phase images were captured by a high-speed camera, which was synchronized with the MIR pulses by a microcontroller.

To characterize WOMiM, we used what we refer to as "on-off-level synchronization". Here, the camera exposure was synchronized to the "on" or "off" state of the OPO: a MIR-ON image was captured when the OPO has been active for 4 s, and a MIR-OFF image was captured 4 s after the OPO has stopped. The exposure time of both MIR-OFF and MIR-ON image was 250 ms. While the on-off-level synchronization limits the speed for chemical-contrast imaging (due to the time interval of 4 s for heat dissipation), it provides a straightforward method for characterizing and demonstrating the working principle of WOMiM.

Figure 1b depicts the working principle of WOMiM. Subtracting the MIR-OFF image from the MIR-ON image yields a subtraction image (henceforth referred to as "subtraction image") and represents the phase contrast difference after MIR illumination. Here, in a wide FOV (determined by the MIR excitation area) with a high MIR absorption sample "A" and low MIR absorption background "B", the subtraction image shows high contrast for "A" and low contrast for "B".

As validation of the working principle of WOMiM, Figure 1c−e shows a MIR-ON image (at 2850 cm^{-1}) (c), a MIR-OFF image (d), and a subtraction image (e) of TAG drops on a ZnS window. We observed that the contrast of TAG drops was enhanced in the subtraction image (Figure 1e), whereas contrast of the background was reduced. Figure 1f shows the subtraction image of two MIR-OFF images, serving as a control experiment to characterize the robustness of CPCM. The standard deviation of all pixel intensity values of Figure 1f was calculated to be 1.02; this standard deviation indicates that the optical stability of the system is comparable to the unit of intensity of the camera, which can change between 0 and 255 in steps of 1. Moreover, no TAG drops were observed as shown in Figure 1f, suggesting that the contrast of TAG drops in the subtraction image in (e) was caused specifically by MIR absorption properties of the TAG drops.

Figure 1g provides zoom-in views of the smallest observed TAG drop from Figure 1e,f (red dashed rectangles). Figure 1h shows the contrast profiles of red and black dashed lines in (g), used to characterize the resolution and the noise of WOMiM. Full width at half-maximum (fwhm) of this TAG drop profile was 1.85 μm. This value is close to the Abbe diffraction limit of 1.75 μm in the case when using a high NA MIR objective ($d = \lambda/2NA$, where NA = 1 and λ = 3.508 μm). However, benefiting from the pump−probe detection, our results demonstrate that the diffraction limit resolution can be achieved with low NA optics (i.e., a MIR parabolic mirror with NA = 0.062 and a visible objective with NA = 0.4).

Figure 1i−n depicts several subtraction images at different laser power used to characterize the linearity of WOMiM image contrast with MIR flux density (radiant energy per unit time per unit area). We observed an increase in the contrast of TAG drops as the excitation flux density increased from 0.039 to 1.97 $\mu W/\mu m^2$. Figure 1o presents an intensity versus flux density plot of two locations: the TAG drop center and background, as indicated by red and blue arrows, respectively,

in Figure 1n. The plot shows a linear relation between MIR excitation and intensity of the subtraction image. Importantly, we noticed that the chemical contrast is observable at a flux density of 0.39 $\mu W/\mu m^2$, which is ~5 orders of magnitude lower than the flux density of Raman microscopy (15 mW/ μm^2)[24] because Raman microscopy focuses light on a small spot to irradiate the sample. This provides a great potential for reducing cellular phototoxicity.

Figure 1p shows the phase contrast image (MIR-OFF) of a 50 μm FOV with positions of a TAG drop and background marked by a blue and red arrow, respectively. Figure 1q shows an intensity variation plot of the two marked locations with a MIR switch-on time at 1 s; Figure 1r is the corresponding plot with a MIR switch-off time at 1 s. The two intensity variation plots were used to characterize the time scale of the heating and cooling process for the purpose of choosing a proper time interval for capturing MIR-ON and MIR-OFF images. Figure 1q indicates that the intensity of the TAG drop increased immediately after MIR starts, while the background intensity remained stable. Exponential fit of the intensity increase yielded a time constant of 0.48 s for heating, and the exponential fit of the intensity decrease yielded a time constant of 0.79 s for cooling as shown in Figure 1r. The values of 0.48 and 0.79 s indicate that the time interval of 4 s chosen in "on-off-level synchronization" was sufficient for ensuring high contrast in MIR-ON images and avoiding residual heat in MIR-OFF.

3.2. Optothermal Signal Characterization and Hyper-spectral Imaging.
We next performed further functional characterization of our system. Figure 2a shows a diagram of a trigger pulse train used to obtain the optothermal signal in water. As shown in the diagram, "OPO trigger in", which is generated by a microcontroller, was introduced to the OPO with a frequency of 1 kHz to generate MIR pulses. After a delay (referred to as "exposure delay"), "camera trigger in" triggers the camera to acquire images at a frequency of 1 kHz (MIR-ON images). The camera captured 50 MIR-ON and 50 MIR-OFF images, with both sets of 50 images subsequently averaged to increase the SNR. Finally, the subtraction image was obtained by subtracting the averaged MIR-OFF image from the averaged MIR-ON image as before. In this configuration, because each single MIR-ON image was captured as a MIR pulse arrived, this synchronization was referred to as "single-pulse-level synchronization" (see Methods). Here, we can adjust the "exposure delay" to monitor the generation and the dissipation process of a single pulse optothermal signal.

Because cells are cultured in an aqueous environment, knowing the relaxation time of optothermal heat in water is fundamental. However, this critical information has not been previously provided. In order to characterize a single pulse optothermal generation and dissipation in water, six frames with the exposure delay varying from 181.2 to 222.2 μs were acquired (Figure 2b−g). Figure 2b depicts a subtraction image before optothermal contrast generation. The first optothermal contrast image (referred to as "hot spot") was observed at an exposure delay of 189.4 μs (Figure 2c). Due to the thermal dissipation, the hot spot reduced in size over time (Figure 2c−f) and completely disappeared after an exposure delay of 222.2 μs (Figure 2g), suggesting that optothermal contrast lasts ~32.8 μs (222.2−189.4 μs) in water. Figure 2h shows a line profile across the hot spot as shown in Figure 2d, which was used to characterize the diameter of the MIR irradiation area.

The fwhm of the hot spot line profile indicates that MIR irradiated an area of 186.2 μm in diameter. Because the chemical contrast of WOMiM was generated from MIR absorption, this irradiation spot size suggests a chemical-contrast FOV of 186.2 μm. To achieve a bigger FOV, one can increase the area of the MIR irradiation spot by vertically shifting the parabolic mirror. We noticed that in Figure 2c−e, the Gaussian hot spot is flattened in the center, providing a homogeneous chemical-contrast FOV. The flattened Gaussian hot spot results from the compensation of a Gaussian excitation spot and doughnut-shaped contrast provided by the CPCM, which has been confirmed by its simulation (see Figure S2).

Figure 2i depicts a plot of intensity versus time for a pixel as indicated by a yellow arrow in Figure 2c, which was used to illustrate the optothermal contrast at a longer time scale compared with Figure 2b−g. The plot was obtained by setting "exposure delay" as a sequence (start: 9 μs; step: 8.2 μs; stop: 238.6 μs). The six green dots, labeled "b" to "g", present the optothermal signal from Figure 2b−g. As shown in Figure 2i, by applying cubic spline interpolation to the optothermal signal, we obtained a fwhm of ~20 μs. Note that we observed a time delay (189.4 μs) between the trigger pulse of "OPO trigger in" and the optothermal signal, which is due to the OPO's intrinsic electronic delay between the "OPO trigger in" and MIR pulse output.

Figure 2j−l depicts three subtraction images of TAG drops in water when WOMiM was tuned to 2920 (j), 2850 (k), and 2830 cm^{-1} (l) used to validate WOMiM's chemical-contrast imaging ability. We observed an enhanced contrast of TAG drops at 2920 cm^{-1} (Figure 2j), which is known as a strong TAG absorption peak due to the CH bond asymmetry stretch vibration.[23] We also observed the absorption peak of the TAG drops at 2850 cm^{-1} (Figure 2k) assigned to the CH symmetry stretch vibration.[23] Because of weak absorption at 2830 cm^{-1}, TAG drops showed no contrast at this wavenumber (Figure 2l). The three images obtained from three wavenumbers demonstrated WOMiM's ability of bond-selective imaging enabled by tuning the OPO to the corresponding bond vibration wavenumber. Note that the three images in Figure 2j−l were selected from hyperspectral images stack (Figure 2m). Benefiting from the high imaging speed, the acquisition time for this hyperspectral images stack took approximately 0.26 s. According to "single-pulse-level synchronization", the actual acquisition time for each chemical-contrast image (with a FOV of 180 μm) can go down to 1 ms. In this hyperspectral image stack (Figure 2m), we averaged 18 images for each wavelength to increase the SNR.

Figure 2n shows WOMiM spectra of TAG drops as shown in Figure 2j−l and a FTIR spectrum of TAG which was performed as validation. WOMiM spectra were obtained from the z-profile of hyperspectral images (from 2950 to 2830 cm^{-1} with a step of 10 cm^{-1}) with the spectra position indicated by two arrows as shown in Figure 2j. The spectra obtained from WOMiM and FTIR are in good agreement.

4. CONCLUSIONS

Here, we presented WOMiM as a novel modality for high-speed chemical-contrast imaging and validated its usability by imaging TAG drops. Chemical-contrast FOVs up to 180 μm were achieved, which is an area 36 times bigger than the current state-of-the-art wide-field CARS imaging modality (FOV ~30 μm in diameter).[12,22] Furthermore, WOMiM can

provide chemical-contrast imaging speeds up to 1 ms/frame, which is 3 orders of magnitude faster than mechanical point-by-point scanning methods[3−6] and 20 times faster than the galvo-resonant scanning method.

Capturing the phase contrast difference induced by MIR absorption for chemical-contrast imaging is a promising novel technique recently proposed,[13−15] offering unique advantages in imaging speed compared to point-by-point scanning methods. We herein demonstrate for the first time optothermal imaging FOVs of over 180 μm by expanding the MIR excitation area while maintaining high imaging speeds (1 ms/frame). Although it seems straightforward for achieving wider FOVs, expanding the MIR excitation area is not trivial because the flux density over the excitation area decreases by the square of the excitation diameter. Similarly, the optothermal signal also decreases by the square of the excitation diameter, which leads to small phase changes. Detecting the subtle change in the phase contrast requires a robust phase readout method, which is met by the CPCM. The high imaging speed combined with the large FOV might meet the need for imaging highly dynamic processes in cells.[7−9,25,26] Given the high imaging speed, hyperspectral imaging with broad spectral coverage (13 wavelengths in our case) was obtained in 0.26 s with the potential of facilitating the identification of spectral fingerprints of specific biomolecules of interest.

According to optothermal signal characterization as shown in Figure 2b−g, the time interval between a single pulse MIR-ON and MIR-OFF image can be as short as 32.8 μs, by taking Figure 2c as the MIR-ON image and taking Figure 2g as the MIR-OFF image. This transit time suggests that WOMiM can theoretically reach a frame rate of 30,488 Hz with a FOV of 180 μm. To achieve this maximum imaging speed, one could for instance increase the MIR pulse repetition rate to 30,488 Hz. A previous study claimed that 70 kHz can be possible with a relaxation time of 6.9 μs.[13] However, even though cells are cultured in a water environment (culture medium), the critical relaxation time of water was not mentioned in this study and the characterization of relaxation time was performed using oil film (or beads in DMSO). We addressed this fundamental gap in the current study. Moreover, we observed a linear relation between the MIR excitation power and intensity of optothermal contrast as shown in Figure 1i−o. The linear relationship provides a way for quantifying the phase change due to MIR absorption. This linearity may be due to the small temperature change in the sample (within 1°). Both the thermo-optic coefficient (dn/dT) of water and TAG are stable within such a small temperature variation.[27,28]

WOMiM can reduce the trade-off between imaging time and imaging area and achieve hyperspectral imaging in a wide wavelength range. Conventionally, a hyperspectral image cube is obtained by acquiring a complete spectrum for each pixel of the FOV, with the imaging time rapidly increasing as the imaging area expands. For example, hyperspectral imaging of an area with 150 × 150 points requires 22,500 spectra. Given a spectral acquisition time of 0.5 s, the total imaging time for this hyperspectral image cube is 3.125 h,[29] which is too long for imaging dynamic processes because the migration speed of cells is around 0.5 μm/min.[30,31] Using the proposed method, a hyperspectral imaging cube of 350 × 350 points (a FOV of ∼180 μm in diameter) can be obtained with total imaging time of 0.26 s.

When applied on a chemically homogeneous sample, WOMiM generates optical absorption spectra of the sample at every pixel of the excited FOV (MIR irradiation area). This is because, as the sample absorbs the MIR radiation, localized heat is generated at every location of the MIR excitation area due to the optothermal effect, resulting in changes of optical path length at every pixel over the area. However, the CPCM is known for a "shade-off" artifact when measuring homogeneous samples with the contrast weaker in the center, that is, generating spectra of different intensity in the center and edges of the FOV. This "shade-off" artifact is partly compensated by the Gaussian intensity profile of the MIR irradiation (MIR intensity is stronger in the center); additionally, detailed characterization of the phase contrast reference field can be used for post-processing correction of the measured spectra in homogeneous samples.

Moreover, owing to the high imaging speed of up to 1 ms/frame, WOMiM is a potential tool for the investigation of intracellular transport, which requires high temporal resolution. For example, lipid droplets are known to undergo a "saltatory" motion, characterized by abrupt movements and changes in direction.[25] The saltatory motion of many organelles occurs at speeds of μm/s.[7] Investigations of lipid droplets' saltatory motion traditionally rely on lipophilic stains where the imaging acquisition rate is limited by fluorescent signal intensity with a weaker florescent signal requiring longer exposure time for a high SNR.[25] WOMiM could benefit two aspects of intracellular transport research: high imaging speeds can ensure precise localization and tracking of organelles while also minimizing blurriness/motion artifacts due to the saltatory motion.

Importantly, similar to a Zernike phase contrast microscope, the well-known "halo" artifacts were observed in WOMiM. The artifacts can lead to an unexpected peak that may reduce the reliability of the spectrum. However, to minimize this problem, an apodized phase objective or algorithm-based process can be applied.[32−34] Regarding the acquisition time, if taking into account the time needed for data transfer from the camera to PC and OPO wavelength tuning, ∼10 min is needed for acquiring the whole hyperspectral stack of 13 images. This can be improved by technical optimization, such as using onboard averaging for MIR-ON and MIR-OFF images before transferring to the PC.

In summary, this work shows that vibrational imaging can be achieved at unprecedented fast imaging speeds (3 orders of magnitude faster than chemical point-by-point scanning methods and 20 times faster than galvo scanning methods) in a wide FOV (36 times larger than recently reported wide-field CARS imaging) through the pump−probe detection of the optothermal signal, which may meet the important need for hyperspectral imaging of intracellular dynamics in the future.

5. DATA AVAILABILITY

All data are available in the main text or the supplementary materials.

■ ASSOCIATED CONTENT

⑤ Supporting Information

The Supporting Information is available free of charge at https://pubs.acs.org/doi/10.1021/acs.analchem.1c02805.

　　Characterization of the CPCM by simulation and experimental result and characterization of the MIR irradiation area (PDF)

AUTHOR INFORMATION

Corresponding Authors

Miguel A. Pleitez − *School of Medicine, Center for Translational Cancer Research (TranslaTUM), Chair of Biological Imaging, Technical University of Munich, D-81675 Munich, Germany; Institute of Biological and Medical Imaging, Helmholtz Zentrum München (GmbH), D-85764 Neuherberg, Germany;* orcid.org/0000-0002-7379-4409; Email: miguel.pleitez@helmholtz-muenchen.de

Vasilis Ntziachristos − *School of Medicine, Center for Translational Cancer Research (TranslaTUM), Chair of Biological Imaging, Technical University of Munich, D-81675 Munich, Germany; Institute of Biological and Medical Imaging, Helmholtz Zentrum München (GmbH), D-85764 Neuherberg, Germany;* orcid.org/0000-0002-9988-0233; Email: bioimaging.translatum@tum.de

Authors

Tao Yuan − *School of Medicine, Center for Translational Cancer Research (TranslaTUM), Chair of Biological Imaging, Technical University of Munich, D-81675 Munich, Germany; Institute of Biological and Medical Imaging, Helmholtz Zentrum München (GmbH), D-85764 Neuherberg, Germany;* orcid.org/0000-0003-1490-5161

Francesca Gasparin − *School of Medicine, Center for Translational Cancer Research (TranslaTUM), Chair of Biological Imaging, Technical University of Munich, D-81675 Munich, Germany; Institute of Biological and Medical Imaging, Helmholtz Zentrum München (GmbH), D-85764 Neuherberg, Germany*

Complete contact information is available at:
https://pubs.acs.org/10.1021/acs.analchem.1c02805

Author Contributions

T.Y. and M.A.P. contributed equally to this work. M.A.P. created the imaging concept. T.Y. built the imaging system, which includes synchronization of the OPO and camera, automation of hyperspectral imaging, and writing a MATLAB user interface for system control. F.G. prepared the TAG droplets and provided the FTIR spectrum. T.Y. performed all the experiments, analyzed the results, and visualized the figures. M.A.P. and V.N supervised the whole study. All authors edited the manuscript.

Notes

The authors declare the following competing financial interest(s): Vasilis Ntziachristos is an equity owner and consultant at iThera Medical GmbH, member of the Scientific Advisory Board at SurgVision BV / Bracco Sp.A, owner at Spear UG, founder and consultant at I3. Vasilis Ntziachristos and Miguel A. Pleitez are founders of sThesis GmbH (i.Gr.).

REFERENCES

(1) Folick, A.; Min, W.; Wang, M. C. *Curr. Opin. Genet. Dev.* **2011**, *21*, 585−590.

(2) Ji, M.; Orringer, D. A.; Freudiger, C. W.; Ramkissoon, S.; Liu, X.; Lau, D.; Golby, A. J.; Norton, I.; Hayashi, M.; Agar, N. Y. R.; Young, G. S.; Spino, C.; Santagata, S.; Camelo-Piragua, S.; Ligon, K. L.; Sagher, O.; Xie, X. S. *Sci. Transl. Med.* **2013**, *5*, 201ra119.

(3) Pleitez, M. A.; Khan, A. A.; Soldà, A.; Chmyrov, A.; Reber, J.; Gasparin, F.; Seeger, M. R.; Schätz, B.; Herzig, S.; Scheideler, M. *Nat. Biotechnol.* **2019**, *38*, 293.

(4) Kee, T. W.; Cicerone, M. T. *Opt. Lett.* **2004**, *29*, 2701−2703.

(5) van Manen, H.-J.; Kraan, Y. M.; Roos, D.; Otto, C. *Proc. Natl. Acad. Sci. U.S.A.* **2005**, *102*, 10159−10164.

(6) Lim, S.-H.; Caster, A. G.; Leone, S. R. *Phys. Rev. A* **2005**, *72*, 041803.

(7) Shubeita, G. T.; Tran, S. L.; Xu, J.; Vershinin, M.; Cermelli, S.; Cotton, S. L.; Welte, M. A.; Gross, S. P. *Cell* **2008**, *135*, 1098−1107.

(8) Olzmann, J. A.; Carvalho, P. *Nat. Rev. Mol. Cell Biol.* **2019**, *20*, 137−155.

(9) Pol, A.; Martin, S.; Fernandez, M. A.; Ferguson, C.; Carozzi, A.; Luetterforst, R.; Enrich, C.; Parton, R. G. *Mol. Biol. Cell* **2004**, *15*, 99−110.

(10) Bean, B. P. *Nat. Rev. Neurosci.* **2007**, *8*, 451−465.

(11) Verboven, K.; Wouters, K.; Gaens, K.; Hansen, D.; Bijnen, M.; Wetzels, S.; Stehouwer, C. D.; Goossens, G. H.; Schalkwijk, C. G.; Blaak, E. E.; Jocken, J. W. *Sci. Rep.* **2018**, *8*, 4677.

(12) Shen, Y.; Wang, J.; Wang, K.; Sokolov, A. V.; Scully, M. O. *APL Photonics* **2018**, *3*, 116104.

(13) Zhang, D.; Lan, L.; Bai, Y.; Majeed, H.; Kandel, M. E.; Popescu, G.; Cheng, J.-X. *Light Sci. Appl.* **2019**, *8*, 116.

(14) Toda, K.; Tamamitsu, M.; Nagashima, Y.; Horisaki, R.; Ideguchi, T. *Sci. Rep.* **2019**, *9*, 9957.

(15) Tamamitsu, M.; Toda, K.; Shimada, H.; Honda, T.; Takarada, M.; Okabe, K.; Nagashima, Y.; Horisaki, R.; Ideguchi, T. *Optica* **2020**, *7*, 359−366.

(16) Kviatkovsky, I.; Chrzanowski, H. M.; Avery, E. G.; Bartolomaeus, H.; Ramelow, S. *Sci. Adv.* **2020**, *6*, No. eabd0264.

(17) Zou, X. Y.; Wang, L. J.; Mandel, L. *Phys. Rev. Lett.* **1991**, *67*, 318.

(18) Lemos, G. B.; Borish, V.; Cole, G. D.; Ramelow, S.; Lapkiewicz, R.; Zeilinger, A. *Nature* **2014**, *512*, 409−412.

(19) Chekhova, M. V.; Ou, Z. Y. *Adv. Opt. Photon* **2016**, *8*, 104−155.

(20) Webb, K. F.; de Fillipi, G.; Johnston, N. *Microsc. Anal.* **2013**, *27*, 27−32.

(21) Webb, K. F. *J. Microsc.* **2015**, *257*, 8−22.

(22) Duarte, A. S.; Schnedermann, C.; Kukura, P. *Sci. Rep.* **2016**, *6*, 37516.

(23) Coates, J. Interpretation of infrared spectra, a practical approach. *Encyclopedia of Analytical Chemistry: Applications, Theory and Instrumentation*; Wiley, 2006.

(24) Murugkar, S.; Brideau, C.; Ridsdale, A.; Naji, M.; Stys, P. K.; Anis, H. *Opt. Express* **2007**, *15*, 14028−14037.

(25) Welte, M. A. *Curr. Biol.* **2004**, *14*, R525−R537.

(26) Welte, M. A. *Biochem. Soc. Trans.* **2009**, *37*, 991−996.

(27) Gouw, T. H.; Vlugter, J. C. *Fette Seifen Anstrichm.* **1966**, *68*, 544−549.

(28) Kim, Y. H.; Park, S. J.; Jeon, S.-W.; Ju, S.; Park, C.-S.; Han, W.-T.; Lee, B. H. *Opt. Express* **2012**, *20*, 23744−23754.

(29) Salehi, H.; Derely, L.; Vegh, A.-G.; Durand, J.-C.; Gergely, C.; Larroque, C.; Fauroux, M.-A.; Cuisinier, F. J. G. *Appl. Phys. Lett.* **2013**, *102*, 113701.

(30) Yan, J.; Irimia, D. *Technology* **2014**, *2*, 185−188.

(31) Hui, J.; Pang, S. W. *Biosci. Rep.* **2019**, *39*, BSR20181596.

(32) Yin, Z.; Kanade, T.; Chen, M. *Med. Image Anal.* **2012**, *16*, 1047−1062.

(33) Otaki, T. *Opt. Rev.* **2000**, *7*, 119−122.

(34) Nguyen, T. H.; Kandel, M.; Shakir, H. M.; Best-Popescu, C.; Arikkath, J.; Do, M. N.; Popescu, G. *Sci. Rep.* **2017**, *7*, 44034.